metals

MDPI

Article

Tensile Fracture Behavior of 2A14 Aluminum Alloy Produced by Extrusion Process

Yunpeng Meng [1], Hua Zhang [2,*], Xia Li [3,*], Xin Zhou [2], Huajun Mo [4,*], Lifei Wang [1] and Jianfeng Fan [1]

1 Key Laboratory of Interface Science and Engineering in Advanced Materials, Ministry of Education, Taiyuan University of Technology, Taiyuan 030024, China; mengyunpeng0160@link.tyut.edu.cn (Y.M.); wanglifei@tyut.edu.cn (L.W.); fanjianfeng@tyut.edu.cn (J.F.)
2 Institute for Advanced Studies in Precision Materials, Yantai University, Yantai 264005, China; zhouxin@ytu.edu.cn
3 College of Nuclear Equipment and Nuclear Engineering, Yantai University, Yantai 264005, China
4 The First Sub-Institute, Nuclear Power Institute of China, Chengdu 610005, China
* Correspondence: zhanghua@ytu.edu.cn (H.Z.); lixia007@ytu.edu.cn (X.L.); mohjnpic@126.com (H.M.)

Abstract: In this study, the tensile mechanical properties of a 2A14 aluminum alloy produced by extrusion were tested at room temperature to investigate the tensile fracture behavior. The results showed that the tensile fracture of the alloy was mixed intergranular and transgranular ductile fracture, as numerous coarse second-phase particles were distributed in a band along the loading direction, making it prone to microcracking. This was determined to be the main cause of fracture failure of the alloy. In addition, we observed large α-AlFeMnSi(Cu), Al(Fe,Mn)Cu, AlCuMgSi, and Al_2Cu phases in the microstructure of the 2A14 aluminum alloy, and both Al_2Cu second phase and precipitation-free phase zone (PFZ) at the grain boundaries were observed, which made the alloy susceptible to fracture failure and reduced the mechanical properties of the alloy.

Keywords: 2A14 alloy; tensile fracture behavior; microstructure; precipitated phase

check for updates

Citation: Meng, Y.; Zhang, H.; Li, X.; Zhou, X.; Mo, H.; Wang, L.; Fan, J. Tensile Fracture Behavior of 2A14 Aluminum Alloy Produced by Extrusion Process. *Metals* **2022**, *12*, 184. https://doi.org/10.3390/met12020184

Academic Editor: Thomas Niendorf

Received: 26 November 2021
Accepted: 17 January 2022
Published: 19 January 2022

Publisher's Note: MDPI stays neutral with regard to jurisdictional claims in published maps and institutional affiliations.

Copyright: © 2022 by the authors. Licensee MDPI, Basel, Switzerland. This article is an open access article distributed under the terms and conditions of the Creative Commons Attribution (CC BY) license (https://creativecommons.org/licenses/by/4.0/).

1. Introduction

Aluminum alloys are commonly used to manufacture engineering parts for aerospace and transportation applications due to their excellent characteristics, such as low density, high strength, good processing properties, and electrical conductivity; however, they have a limited range of applications, as aluminum alloys lose strength at high temperatures [1,2]. Alloying is an effective way to avoid this issue. For example, Al-Cu alloys have high toughness and excellent mechanical properties at high temperatures [3,4]. Furthermore, adding alloying elements such as Si and Mg to Al-Cu alloy can change the precipitation behavior of the alloy and improve its mechanical properties. 2A14 aluminum alloy is a typical Al-Cu-Si-Mg forged aluminum alloy with high strength, heat resistance, and good thermoplasticity, and hence, it is used for forging and drop-forged parts subjected to heavy loads [5–9]. 2A14 aluminum alloy is also a heat-treatment-strengthening alloy, and its mechanical properties can be improved by heat treatment. Of these, solution and artificial aging (T6) are the heat treatment processes that can maximize the strength of this alloy [10].

Researchers are increasingly studying 2A14 aluminum alloy. Wang et al. [11] investigated the effect of accumulated strain on the microstructure evolution and mechanical properties of the 2A14 aluminum alloy. In addition, Lan et al. [12] subjected a 2A14 aluminum alloy to cold deformation and subsequent aging treatments, and then analyzed the strengthening mechanism of the 2A14 aluminum alloy with different cold deformations during aging. Zhang et al. [7] investigated the effect of the cooling rate on the residual stresses and tensile properties of 2A14 aluminum alloy forging through numerical simulations and quenching experiments. However, few reports have investigated and analyzed the room-temperature tensile fracture behavior of 2A14 aluminum alloy. Thus, by studying the fracture type and fracture mechanism of 2A14 aluminum alloy materials at room temperature and determining the cause of fracture failure, the preparation process of 2A14 aluminum alloy can be optimized. In addition, because of its potential applications, it is essential to study the tensile fracture behavior of 2A14 aluminum alloy to ensure its safety.

The distribution, size, and number of second-phase particles in precipitate phase reinforced Al-Cu-Si-Mg alloys are essential to their mechanical properties. The strengthening phase of this alloy type varies with the amount and type of alloying elements. Cu tends to form the θ-Al_2Cu phase in the aluminum matrix when Mg content is low and Cu content is high. Studies have shown that the strengthening phase of Al-Cu-Mg alloys is influenced by the C_{Cu}/C_{Mg} atomic concentration ratio, and when the C_{Cu}/C_{Mg} atomic concentration ratio is too large, the θ-Al_2Cu phase and its transition phase are the main strengthening phases [12,13]. Thus, the distribution and morphology of the θ phase and its transition phase are critical for Al-Cu-Si-Mg-type alloys. In addition, the distribution and size of the second phase will affect the fracture behavior of the alloy. Therefore, it is important to systematically study the second phase of the 2A14 aluminum alloy after tensile fracture.

In this study, we assessed the tensile fracture behavior of the 2A14 aluminum alloy at room temperature and determined the second phase type and distribution in its microstructure, and the precipitated phases and their effects on the properties of the alloy were assessed by energy dispersive spectrometer (EDS) and transmission electron microscope (TEM). Moreover, the fracture mechanism of the 2A14 aluminum alloy provides a theoretical and practical basis for further research and development of 2A14 aluminum alloy materials.

2. Experimental Section

The actual and reference chemical compositions of the 2A14 aluminum alloy used in this study are shown in Table 1. Experimentally, the 2A14 aluminum alloy needs to be cooled in water after solution treatment at 495 °C for 1 h and then cooled by air after aging treatment at 160 °C for 10 h to achieve peak properties of the 2A14 aluminum alloy. Figure 1 shows the microstructure of the 2A14-T6 alloy. It can be seen that the grains elongate along the extrusion direction and are surrounded by recrystallized grains, and the average grain size is measured to be 22.5 (±0.3) μm, and the transversal average size and longitudinal average size of the crystal grains are 35.5 (±0.5) and 9.5 (±0.2) μm, respectively. There are large-sized precipitates in the metal matrix, which will hinder the movement of dislocations in the 2A14 aluminum alloy material so that it has good mechanical properties.

Table 1. Actual and reference chemical composition of the 2A14 aluminum alloy (wt.%).

Composition	Cu	Mg	Si	Mn	Ni	Zn	Fe	Ti	Al
Actual	4.68	0.629	0.980	0.973	0.0098	0.042	0.155	0.0026	Bal.
Reference	3.9–4.8	0.4–0.8	0.6–0.12	0.4–1.0	<0.1	<0.3	<0.7	<0.16	Bal.

The metallography of the 2A14 aluminum alloy was obtained by etching with Keller's reagent and observed by an optical microscope (OM). The microstructure and tensile fracture of the 2A14 aluminum alloy were observed by scanning electron microscopy (SEM, JSM-6700, JEOL, Tokyo, Japan, 20 kV). The composition in the microstructure of the 2A14 aluminum alloy was initially determined using EDS. The microstructure was observed by TEM (JEM-2010, JEOL, Tokyo, Japan, 200 kV) and further analyzed for the second phase. The 2A14 aluminum alloy is machined into a dog bone-shaped tensile specimen with a diameter of 5 mm and a standard length of 25 mm according to ASTM E8M-04 (Tensile test method for metallic materials, USA). CMT5205 (MTS, Eden Prairie, MN, USA) universal testing machine was used to test tensile mechanical properties at room temperature with a strain rate of 1×10^{-3} s^{-1}. Each group of mechanical experiments was repeated three times to ensure the accuracy of experimental data.

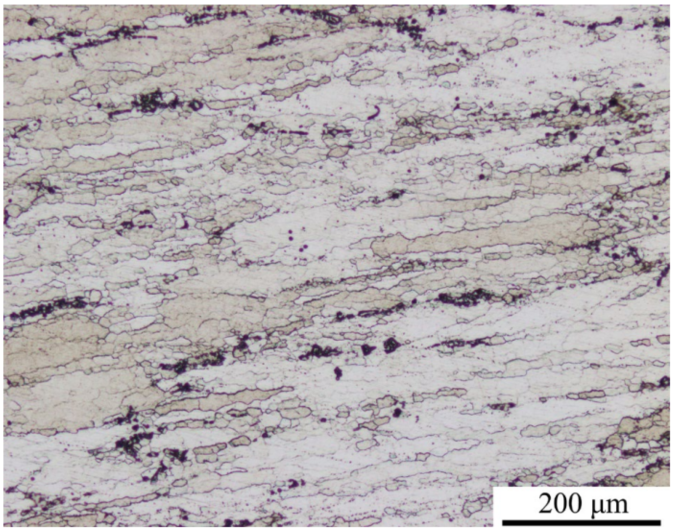

Figure 1. OM (optical microscope) micrograph of 2A14-T6 aluminum alloy.

3. Results and Discussions

3.1. Tensile Properties

Figure 2 shows the tensile stress–strain curve of the 2A14 aluminum alloy. The calculated yield strength value was 445 (±2) MPa, the tensile strength was 485 (±5) MPa, the elongation after fracture was 7 (±0.2) %, and the elastic modulus was 69.43 GPa.

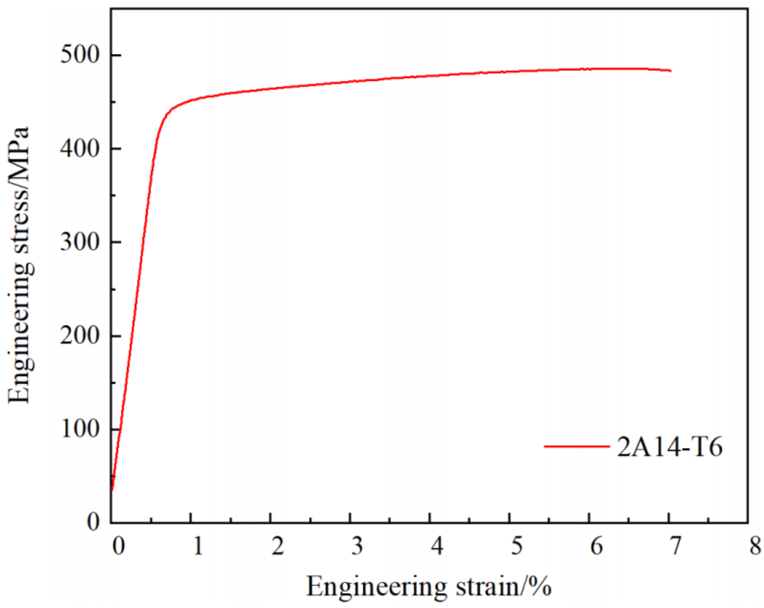

Figure 2. Engineering stress–strain curve of the 2A14 aluminum alloy.

3.2. Longitudinal Section Morphology of Fracture

As shown in Figure 3a, the longitudinal section of the tensile fracture sample along the loading direction indicated that the fracture was ~60° from the loading direction. Therefore, the fracture surface was rough and uneven, with slight shrinkage in the cross-section at the location of fracture, which was determined to be ductile fracture. In the enlarged areas, labeled as 1 and 2 in Figure 3a, we observed an obvious intergranular fracture phenomenon in the local microstructure, discernable as a band-like distribution (shown by the arrow in Figure 3b,c), particle fragmentation (shown by the black arrow in Figure 3a(2)), and particle and matrix debonding, which caused microcrack initiation and promoted crack propagation until fracture. This was attributed to the continuity of grain boundaries, which were destroyed when the brittle second-phase and inclusion became attached to the grain boundaries, leading to intergranular fracture of the metal. In addition to the banded distribution of numerous coarse second-phase particles along the extrusion direction, Figure 3b shows that the grain structure exhibited fibrous banded distribution, indicating that complete recrystallization did not occur in the alloy.

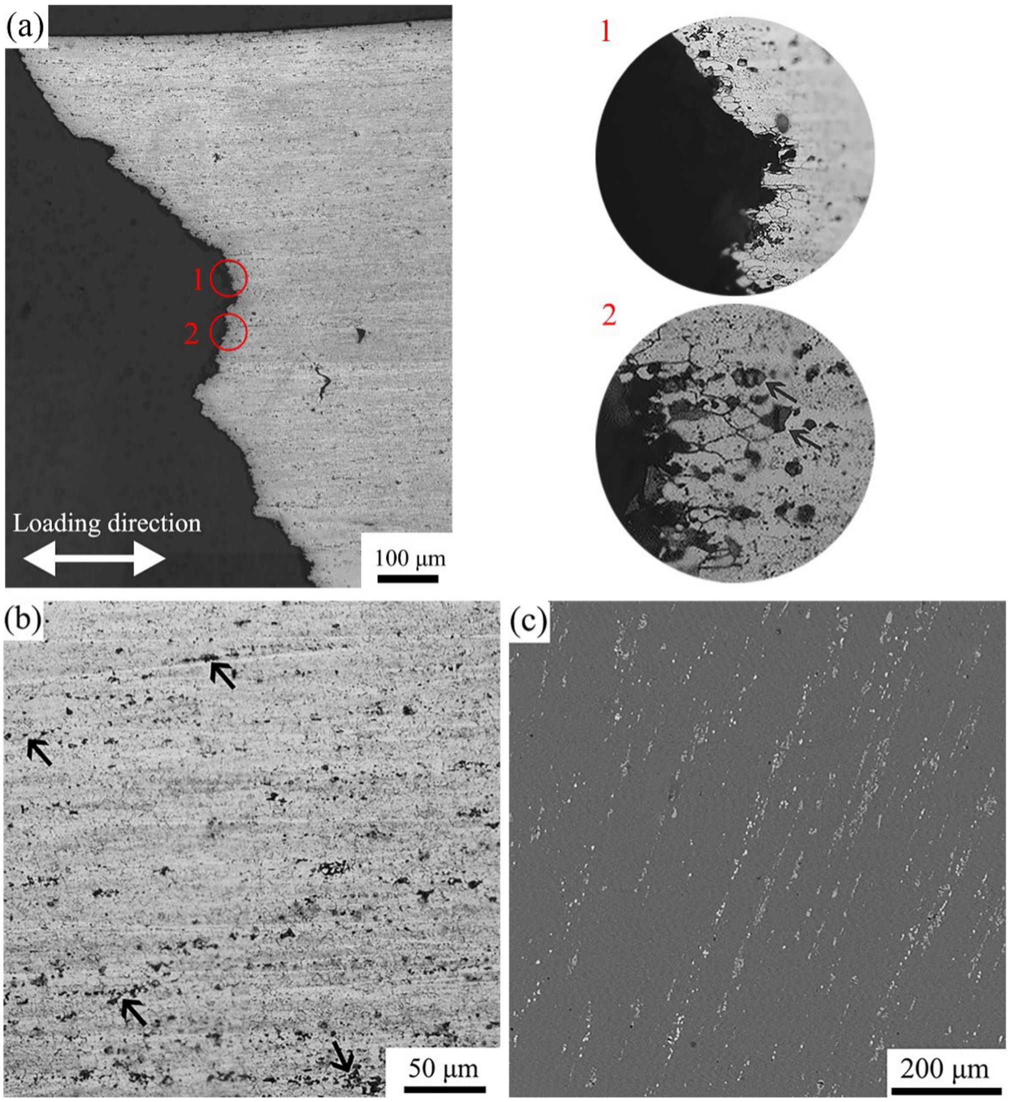

Figure 3. Morphology and microstructure of the longitudinal fracture section, where (**a**,**b**) are the OM micrograph, and (**c**) shows the SEM micrograph. (Observation positions 1 and 2 in Figure (**a**) at high magnification, the arrows refer to the second phase in the microstructure).

The second-phase particle composition was also analyzed. As shown in Figure 4, the microstructure of the 2A14 aluminum alloy mainly consisted of light gray and bright white phases (labeled by 1 and 2, respectively). The map scanning results showed that the bright white phase mainly contained Cu elements, while the light gray phase mainly contained Fe, Mn, and Si elements. The second phase in the Al-Cu-Si-Mg alloy was mainly divided into two categories: the first phase contained Fe impurity elements, and was difficult to dissolve and transform, such as AlFeMnSi and AlCuFe phases [14]; the other phase dissolved and transformed after heat treatment, and mainly consisted of Al_2Cu and Al_2CuMg phases [15]. Therefore, we concluded that the bright white phase was the Al_2Cu phase, and the light gray phase was the α-AlFeMnSi phase. For Al-Cu alloy, the θ-Al_2Cu phase and its transition phase were the main precipitate-strengthening phases [12]. The above experimental results also showed a large stable θ-Al_2Cu phase in the alloy, which reduced the solid Cu solubility in the Al matrix and affected the subsequent age strengthening effect. This was possibly related to the homogenization and solution treatment system, which did not completely dissolve or redissolve the θ-Al_2Cu phase.

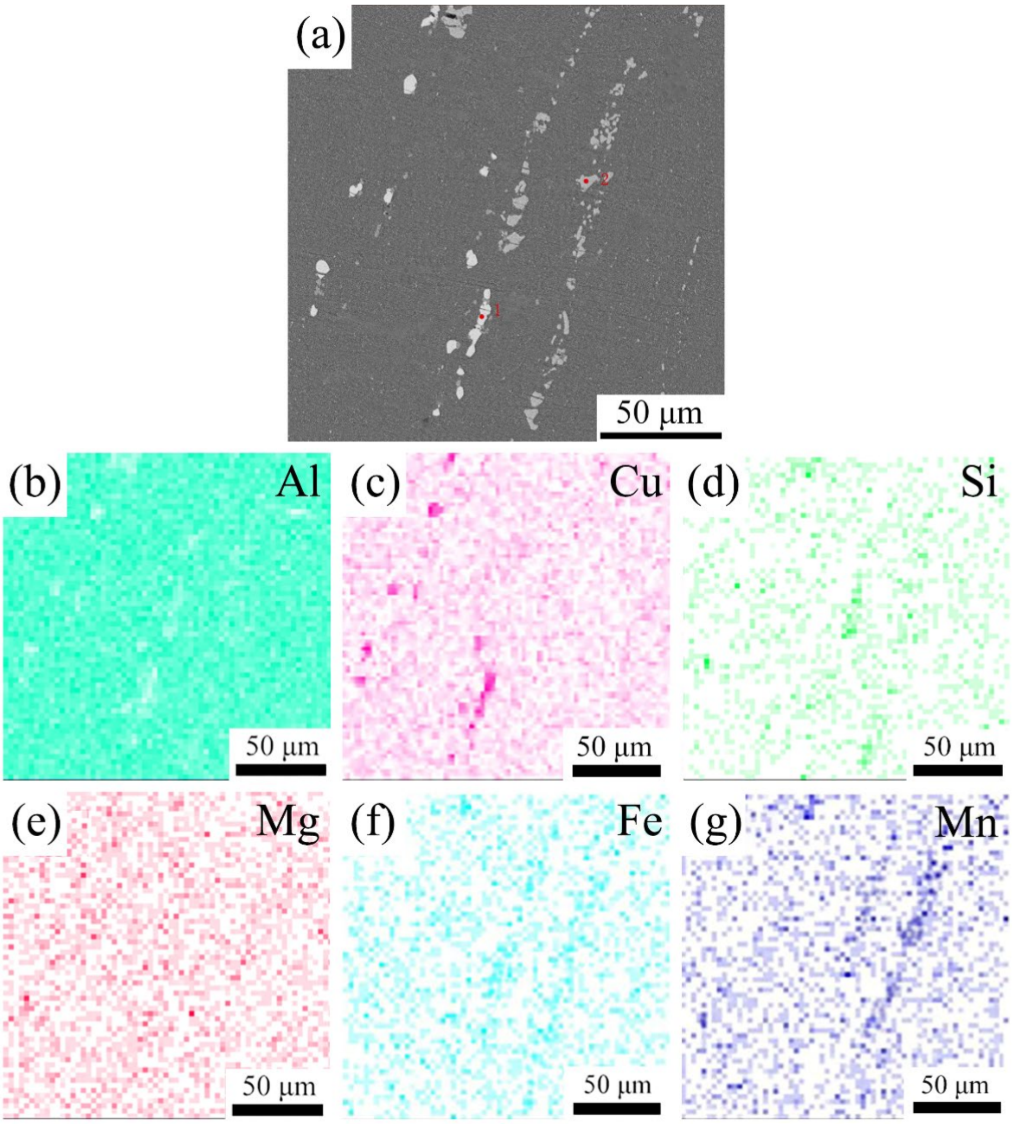

Figure 4. (**a**) Backscattered electrons (BSE) micrograph, (**b**–**g**) mapping of Al, Cu, Si, Mg, Fe and Mn. (2D distribution of elements determined using EDS).

3.3. Fracture Appearance

As shown in Figure 5a–d, the fracture morphology of the 2A14 aluminum alloy exhibited obvious dimple fracture characteristics, and no intergranular fracture features were found. However, the longitudinal fracture section indicated intergranular fracture, and according to the alloy grain group, the fracture surface morphology can be determined. The tensile fracture of the 2A14 aluminum alloy is intergranular, and transgranular fracture consisted of mixed ductile fracture; however, the dimples were relatively shallow, indicating the poor tensile plasticity of the alloy. Due to the presence of numerous coarse second-phase particles in the alloy, the micro-cracks led to, and promoted, crack propagation, and a larger number of fracture particles were observed on the alloy fracture surface, as shown by the red arrows in Figure 5c. Moreover, the fracture morphology of the BSE showed the obvious band-like distribution of the second phase particles (as shown in Figure 5e), which was consistent with the previous metallographic structure results.

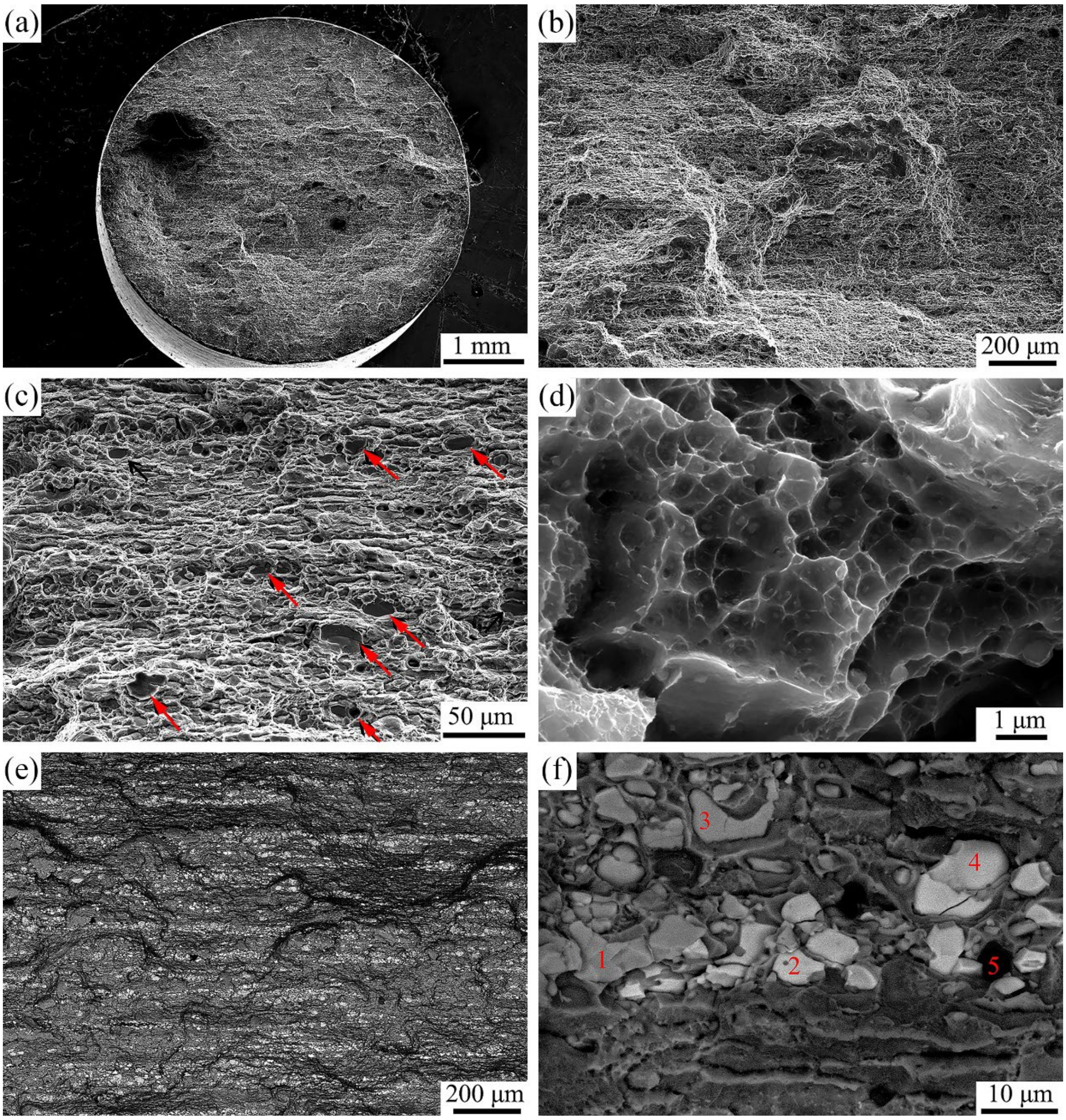

Figure 5. Fractography of a tensile specimen. (**a**–**d**) Second electron (SE) micrographs, (**e**–**f**) BSE micrographs. (The red arrows in (**c**) are dimples, the numbers 1–5 in (**f**) refer to different second phases).

As shown in Figure 5f and Table 2, light gray area 1 contained Al, Si, Mn, Fe, Cu elements, and light gray area 3 contained Al, Mn, Fe, Cu elements. Therefore, we determined that the light gray phases, 1 and 3, were α-AlFeMnSi(Cu) and Al(Fe, Mn)Cu phases, respectively. Bright white area 2 contained Al, Si, Mg, and Cu elements, and was possibly an AlCuMgSi phase (Q phase), while bright area 4 mainly contained Al and Cu elements, which were possibly the AlCu phase. In addition, black area 5 contained Al and Cu, and a small amount of Mg elements, and was tentatively determined to be the AlCuMg phase. However, further phase analysis is needed to determine the final phase composition.

Table 2. EDS analysis results of areas 1–5 in Figure 5f (wt.%).

Point	Mg	Al	Si	Mn	Fe	Cu
1	-	55.50	7.79	19.70	9.95	7.06
2	11.27	39.07	10.36	-	-	38.60
3	0.63	37.10	1.13	29.97	17.15	13.66
4	0.31	15.04	-	-	-	84.42
5	1.02	82.90	-	-	-	16.08

3.4. TEM Microstructure Analysis

According to the above OM and SEM results, numerous coarse second-phase particles were mainly distributed at the grain boundaries, and were the main cause of microcracks and fracturing. This was attributed to tensile deformation, which occurs at room temperature, and dislocations will proliferate and accumulate in the coarse secondary interactions within the grain or grain boundaries. In addition, stress concentrations will form locally, leading to microcrack initiation, and these cracks will continue to expand and converge to form a main crack, until fracture. Studies have shown that with more precipitated phases at grain boundaries, cavities and cracks will generate more easily around coarse grain boundary particles [16,17]. The second-phase near the grain boundary was further characterized by TEM, as shown in Figure 6, revealing the presence of spherical, irregular, and striped phases. Point component analysis of the A–E phases in the TEM microstructure, as shown in Figure 6a–c, was conducted separately and the results are presented in Figure 6 and Table 3. We concluded that A, C, and D were the α-AlFeMnSi(Cu) phase (Fe-rich phase, size 0.3–1 μm), B was the Al_2Cu phase (length ~2.3 μm, width ~1.2 μm), and E was the Q-$Cu_2Mg_8Si_6Al_5$ phase (size ~2 μm). Combined with the SEM and TEM characterization results, the second-phase particles in the alloy mainly consisted of α-AlFeMnSi(Cu), Al_2Cu, and Q-$Cu_2Mg_8Si_6Al_5$ phases, and possibly Al(Fe,Mn)Cu and AlCuMg phases, which also require further characterization and verification.

In addition, the TEM results showed numerous light-colored 100~200 nm particles in the grains (as shown in Figure 7a,b), black ~0.5 μm particles and strips 0.5~1 μm in length at the grain boundary (as shown in Figure 7a,c,d). The compositional analysis results showed that the black particulate phase was an Fe-rich phase (A in Figure 7c), while the stripe phase was the θ-Al_2Cu phase (B in Figure 7c,d), and the light-colored particulate was Q-$Cu_2Mg_8Si_6Al_5$. The Q-$Cu_2Mg_8Si_6Al_5$ phase will precipitate during the aging of Al-Mg-Si-Cu alloys, and has a strengthening effect on the alloy, due to the synergistic strengthening effects between the θ-Al_2Cu and Q-$Cu_2Mg_8Si_6Al_5$ phases [18,19]. As shown in Figure 7c,d, in addition to the particulate or stripe phases, brightly colored PFZ was present at the grain boundary in the alloy. This presence of PFZ could also affect the mechanical and electrochemical corrosion properties of the grain boundary micro-zones, and affect the fracture failure and corrosion resistance of the alloy. Because the PFZ was soft, dislocations could proliferate and accumulate at the second-phase grain boundaries and the PFZ, resulting in local stress concentrations, and cavities, which can preferentially form, grow, and converge in the PFZ, exhibiting characteristics of intergranular fracture. Meng et al. [20] showed that the strength of the PFZ was lower than matrix, leading to additional strain localizations and the destruction of grain boundaries. Similarly, reports in the literature have shown that PFZ formation and growth near grain boundaries can reduce the mechanical properties of the alloy [21,22]. In addition, this process can be regulated and optimized for specific service performance requirements, such as strength, toughness, and corrosion resistance.

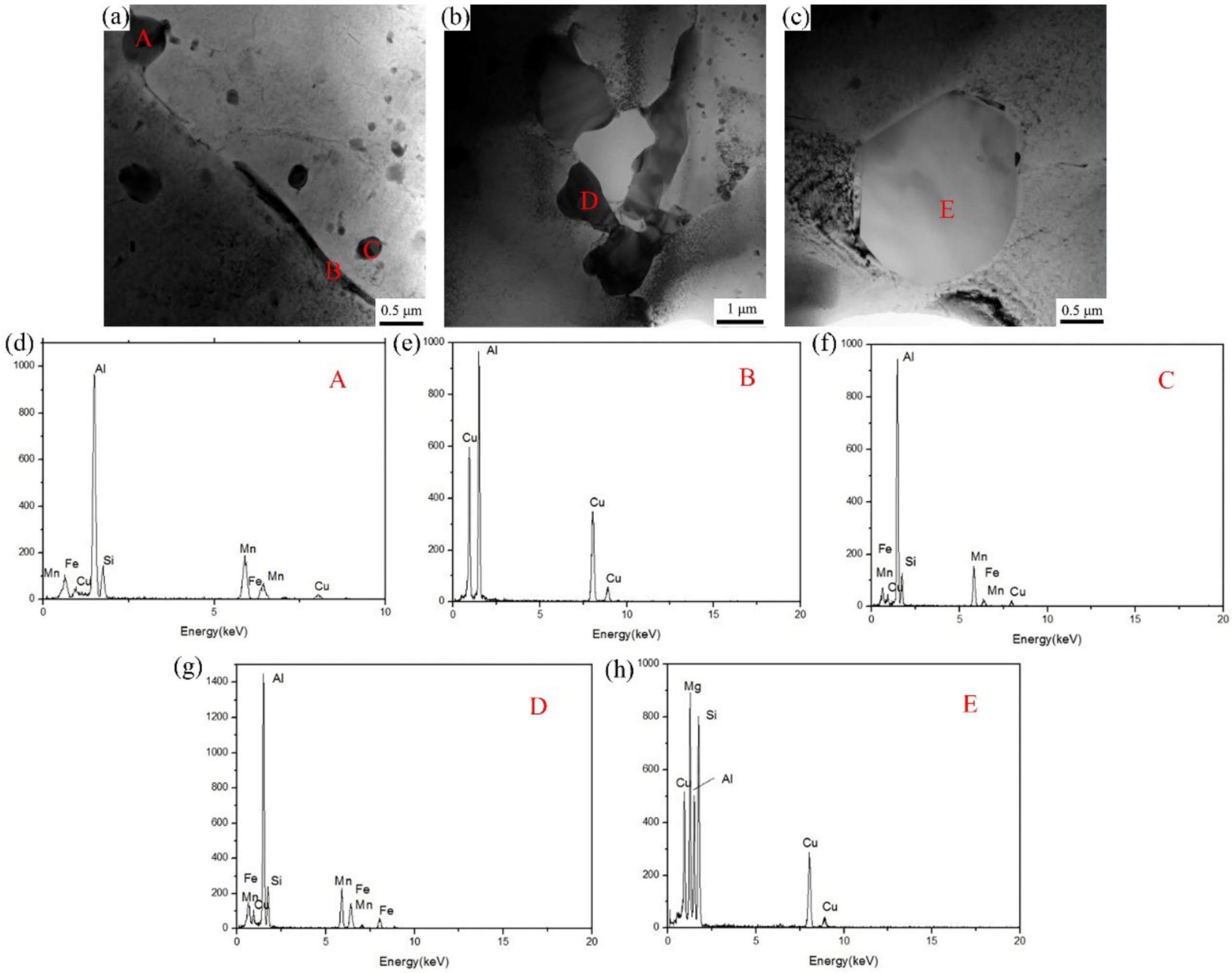

Figure 6. (**a**–**c**) Bright-field TEM micrographs; (**d**–**h**) EDS spectra of phases indicated in (**a**–**c**). (**A**–**E**) are the different phases in Figure 6 (**a**–**c**).

Table 3. Energy spectrum analysis of grain boundary phase composition (wt.%) from Figure 6.

Point	Al	Si	Mn	Fe	Cu	Mg
A	61.43	8.38	21.78	5.48	2.91	-
B	50.41	-	-	-	49.89	-
C	68.15	8.26	19.27	1.38	2.92	-
D	56.42	9.68	16.8	11.7	5.91	-
E	17.48	28	-	-	23.63	30.87

The mechanical properties of the Al-Cu alloy can be improved mainly by precipitation strengthening; thus, the uniform distribution of the fine θ′-Al_2Cu metastable phase or GP region can be obtained by reasonable aging treatments to strengthen the Al matrix, forming numerous precipitates in the aged Al-Cu alloy matrix. Figure 8 shows many fine needle-like phases (three-dimensional structure may be a sheet) that precipitated in the alloy matrix, and were uniformly distributed in the matrix. The precipitated phases also grew in two mutually perpendicular directions (Figure 8a). The data showed that the precipitate was 15~130 nm in length, 3~10 nm in width, and the volume fraction was about 4.2%. The diffraction areas are shown in Figure 8d, indicating that the precipitated phase in the matrix was the θ′-Al_2Cu phase.

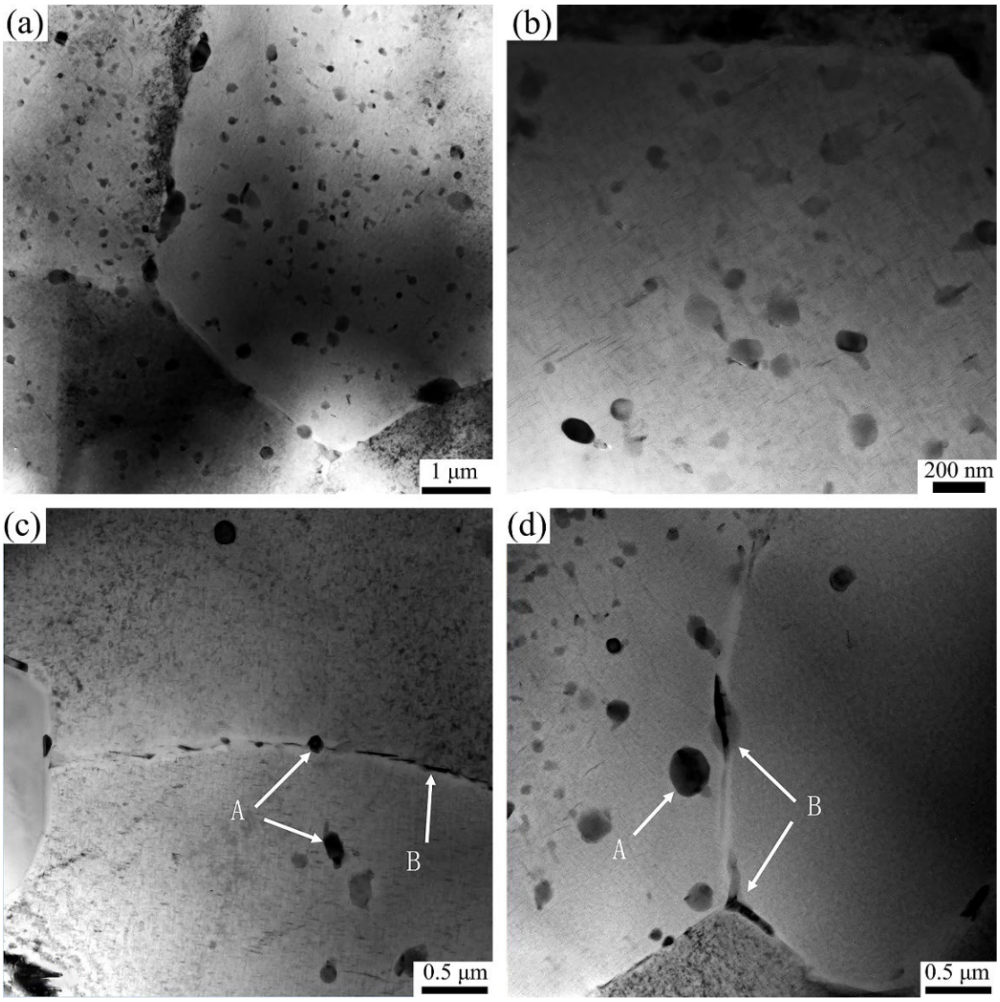

Figure 7. TEM images showing grain boundary and intracrystalline phases. (**a**,**b**) show the distribution of phases. The morphologies of the grain boundary and intragranular phases are shown in (**c**,**d**).

The high-resolution results images showed that the width of the precipitated phase increased from several atomic layers (1–4 in Figure 8e,f) to several nanometers, and then to more than ten nanometers (5–6 in Figure 8f), and the precipitated phase was coherent with the matrix. The precipitated phase gradually grew from initial atomic clusters, forming areas 1–4, and then continued to grow, forming areas 5–6. The precipitated phase grew in both length and width, but its length grew more rapidly. Reports have shown that the precipitation sequence of the θ phase follows: SSS → GP region → θ″ phase → θ′ phase → θ′ phase, where SSS is a supersaturated solid solution [23,24]. Therefore, the θ′ phase formed after the formation of the θ′ phase, with the enrichment of copper atoms. The θ′ phase was the transition phase of θ and had a tetragonal lattice. The coherent relationship between the θ′ phase and the matrix was maintained by the {100} plane. When the coherent relationship between the θ′ phase and the matrix started to dissociate, the coherent relationship became semi-coherent, causing the alloy to soften. With the formation and growth of the θ phase, the θ phase completely dissociated from the coherent relationship with the matrix, and the strength of the alloy continued to decrease.

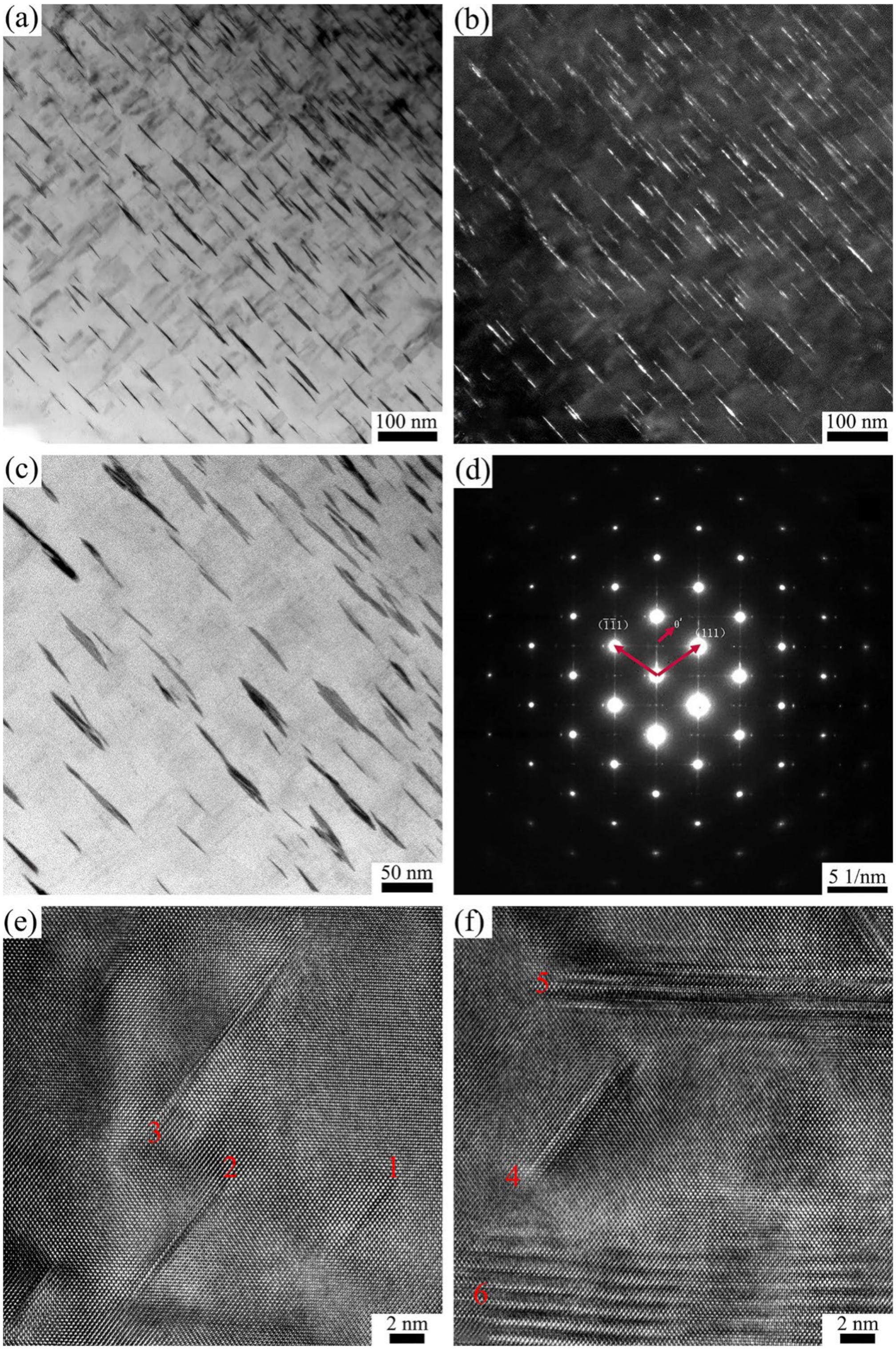

Figure 8. TEM bright field (**a**,**c**) and dark field (**b**) images, with selected diffraction spots (incident direction [011] Al) (**d**), and high-resolution images (**e**,**f**) of the precipitates in the intracrystalline phase.

Considering the microstructure characteristics of the grain boundary precipitates and the PFZ, as shown in Figure 8c,d, the HAADF (High-angle annular dark field) imaging mode was used to characterize and analyze the grain boundary region, and the analysis results were shown in Figure 9. The precipitates at the grain boundaries were discontinuous (particulate or short bar), and there was no obvious precipitation at the junction between the precipitates at the grain boundaries and the ingrain, as shown in Figure 9a,b. Figure 9b also shows the scanning results of line 1, indicating that Al decreased, Mg and Si increased significantly, Cu slightly increased, and Fe and Mn remained mostly unchanged in the discontinuous precipitate phase at the grain boundary. Thus, Mg, Si, and a small amount of Cu underwent grain boundary segregation. Grain boundary segregation mainly occurred during the solid solution treatment and quenching processes of the alloy, resulting in lower concentrations of Mg, Si, and Cu in the matrix than at the grain boundary [25,26]. The scanning results for line 2 showed that the bright white phase at the grain boundary mainly contained Cu elements; therefore, we determined this phase to be the Al_2Cu phase. According to the elemental distribution in the line scan image, the width of the PFZ was approximately 100 nm. After comparing Figure 9c,d, the main difference was the varying degrees of Cu enrichment. This indicated that the grain boundary segregation of Mg, Si, and a small number of Cu elements in the PFZ at the grain boundary may be a common phenomenon.

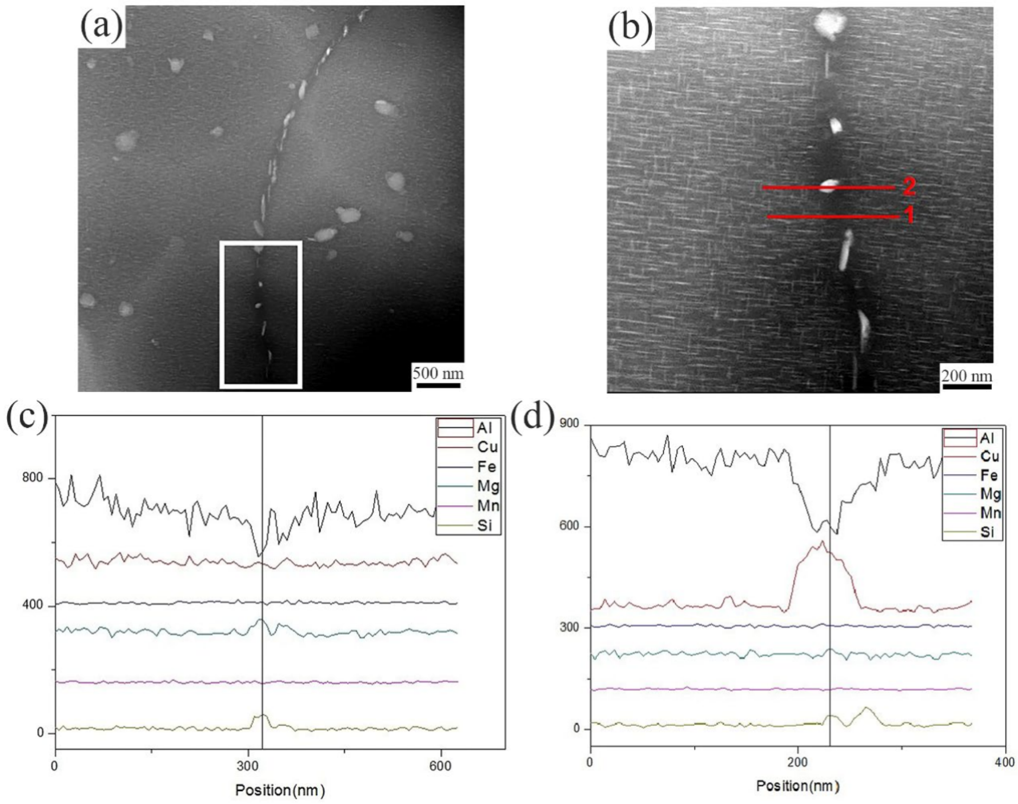

Figure 9. TEM-HAADF images of the grain boundaries and inner-grain precipitates (**a**,**b**, where **b** is the enlargement of the white square area in **a**). The grain boundaries were scanned along the composition lines, shown as red lines 1 (**c**) and 2 (**d**) in (**b**).

4. Conclusions

(1) The tensile fracture mode of the 2A14 aluminum alloy was mixed intergranular and trans-granular ductile fracture. Specifically, numerous coarse second-phase particles were distributed along the loading direction which readily induced microcracks, and these mainly caused the fracture failure of the alloy.

(2) The coarse second-phase mainly consisted of α-AlFeMnSi (Cu), Al (Fe, Mn) Cu, AlCuMgSi, and Al_2Cu phases. The presence of the latter two phases indicated that some of the Cu elements did not participate in the aging strengthening phase. Thus, the homogenization and solid solution process of the alloy may possibly be optimized.

(3) The precipitated phase in grain was metastable θ'-Al_2Cu phase with a length of 15~130 nm and a width of 3~10 nm. There were significant Al_2Cu precipitates and PFZ at

the grain boundary, which can easily affect the fracture failure and corrosion resistance of the alloy.

Author Contributions: Investigation, Y.M. and X.L.; Project administration, H.Z.; Writing (original draft) Y.M.; Supervision, H.Z.; Writing (review and editing), H.Z., X.L., X.Z., H.M. and L.W.; Formal analysis, H.M. and J.F. All authors have read and agreed to the published version of the manuscript.

Funding: This study was supported by National Natural Science Foundation of China (U1810122, U1710118 and 51704209), Yantai high-end talent introduction "Double Hundred Plan" (2021), Talent Training Program for Shandong Province Higher Educational Youth Innovative Teams (2019), Key Research and Development Program of Shanxi Province (201903D421076 and 201803D421086), Innovative Talents of Higher Education Institutions of Shanxi (2018).

Institutional Review Board Statement: Not applicable.

Informed Consent Statement: Not applicable.

Data Availability Statement: All data included in this study are available upon request by contact with the corresponding author.

Acknowledgments: The authors declare that all the support is covered by the author contribution or funding sections.

Conflicts of Interest: The authors declare that they have no known competing financial interests or personal relationships that could have appeared to influence the work reported in this paper.

References

1. Ghosh, S.K. Influence of cold deformation on the aging behaviour of Al-Cu-Si-Mg Alloy. *J. Mater. Sci. Technol.* **2011**, *27*, 193–198. [CrossRef]
2. Ammar, H.R.; Baig, M.; Seikh, A.H.; Mohammed, J.A. Effect of alloying elements on thermal stability of nanocrystalline Al alloys. *Trans. Nonferr. Metal. Soc.* **2021**, *31*, 11–23. [CrossRef]
3. Rodrigues, A.V.; Lima, T.S.; Vida, T.A.; Brito, C.; Garcia, A.; Cheung, N. Microstructure features and mechanical/electrochemical behavior of directionally solidified Al-6wt.%Cu-5wt.%Ni alloy. *Trans. Nonferr. Metal. Soc.* **2021**, *31*, 1529–1549. [CrossRef]
4. Cai, Q.; Mendis, C.L.; Wang, S.; Chang, I.T.H.; Fan, Z. Effect of heat treatment on microstructure and tensile properties of die-cast Al-Cu-Si-Mg alloys. *J. Alloys Compd.* **2021**, *881*, 160559. [CrossRef]
5. Wang, J.; Lu, Y.; Zhou, D.; Sun, L.; Xie, L.; Wang, J. Mechanical properties and microstructural response of 2A14 aluminum alloy subjected to multiple laser shock peening impacts. *Vacuum* **2019**, *165*, 193–198. [CrossRef]
6. Zhang, H.; Wang, M.; Zhang, X.; Yang, G. Microstructural characteristics and mechanical properties of bobbin tool friction stir welded 2A14-T6 aluminum alloy. *Mater. Design* **2015**, *65*, 559–566. [CrossRef]
7. Zhang, Y.; Yi, Y.; Huang, S.; Dong, F. Influence of quenching cooling rate on residual stress and tensile properties of 2A14 aluminum alloy forgings. *Mater. Sci. Eng. A* **2016**, *674*, 658–665. [CrossRef]
8. Kent, D.; Schaffer, G.B.; Drennan, J. Age hardening of a sintered Al-Cu-Mg-Si-(Sn) alloy. *Mater. Sci. Eng. A* **2005**, *405*, 65–73. [CrossRef]
9. Wang, F.; Zeng, Y.; Xiong, B.; Zhang, Y.; Li, X.; Li, Z.; Liu, H. Effect of Si addition on the microstructure and mechanical properties of Al-Cu-Mg alloy. *J. Alloys Compd.* **2014**, *585*, 474–478. [CrossRef]
10. Huang, L.; He, L.; Chen, S.; Chen, K.; Li, J.; Li, S.; Liu, W. Effects of non-isothermal aging on microstructure, mechanical properties and corrosion resistance of 2A14 aluminum alloy. *J. Alloys Compd.* **2020**, *842*, 155542. [CrossRef]
11. Wang, M.; Huang, L.; Liu, W.; Ma, Y.; Huang, B. Influence of cumulative strain on microstructure and mechanical properties of multi-directional forged 2A14 aluminum alloy. *Mater. Sci. Eng. A* **2016**, *674*, 40–51. [CrossRef]
12. Lan, J.; Shen, X.-J.; Liu, J.; Hua, L. Strengthening mechanisms of 2A14 aluminum alloy with cold deformation prior to artificial aging. *Mater. Sci. Eng. A* **2019**, *745*, 517–535. [CrossRef]
13. Wang, B.; Yi, Y.; He, H.; Huang, S. Effects of deformation temperature on second-phase particles and mechanical properties of multidirectionally-forged 2A14 aluminum alloy. *J. Alloys Compd.* **2021**, *871*, 159459. [CrossRef]
14. Strake, E.A.; Stakey, J.T. Application of modern aluminum alloys to aircraft. *Prog. Aerosp. Sci.* **1996**, *32*, 131–172. [CrossRef]
15. Xue, W.; Wang, C.; Li, Y.; Deng, Z.; Chen, R.; Zhang, T. Effect of microarc discharge surface treatment on the tensile properties of Al-Cu-Mg alloy. *Mater. Lett.* **2002**, *56*, 737–743. [CrossRef]
16. Vasudévan, A.K.; Doherty, R.D. Grain boundary ductile fracture in precipitation hardened aluminum alloys. *Acta Metall.* **1987**, *35*, 1193–1219. [CrossRef]
17. Kirman, I. The relation between microstructure and toughness in 7075 aluminum alloy. *Metall. Trans.* **1971**, *2*, 1761–1770.
18. Zhu, X.; Dong, X.; Blake, P.; Ji, S. Improvement in as-cast strength of high pressure die-cast Al-Si-Cu-Mg alloys by synergistic effect of Q-Al5Cu2Mg8Si6 and θ-Al2Cu phases. *Mater. Sci. Eng. A* **2021**, *802*, 140612. [CrossRef]

19. Zafar, S.; Ikram, N.; Shaikh, M.; Shoaib, K. Microstructure studies in Al-6% Si-1.9% Cu-x% Mg alloys. *J. Mater. Sci.* **1990**, *25*, 2595–2597. [CrossRef]
20. Chen, L.; Yan, A.; Liu, H.; Li, X. Strength and fatigue fracture behavior of Al-Zn-Mg-Cu-Zr(-Sn) alloys. *Trans. Nonferr. Metal. Soc.* **2013**, *23*, 2817–2825. [CrossRef]
21. Cai, B.; Adams, B.L.; Nelson, T.W. Relation between precipitate-free zone width and grain boundary type in 7075-T7 Al alloy. *Acta Mater.* **2007**, *55*, 1543–1553. [CrossRef]
22. Lütjering, G.; Albraecht, J.; Sauer, C.; Krull, T. The influence of soft, precipitate-free zones at grain boundaries in Ti and Al alloys on their fatigue and fracture behavior. *Mater. Sci. Eng. A* **2007**, *468–470*, 201–209. [CrossRef]
23. Ringer, S.P.; Sofyan, B.T.; Prasad, K.S.; Quan, G.C. Precipitation reactions in Al-4.0Cu-0.3Mg (wt.%) alloy. *Acta Mater.* **2008**, *56*, 2147–2160. [CrossRef]
24. Bassani, P.; Gariboldi, E.; Vimercati, G. Calorimetric analyses on aged Al-4.4Cu-0.5Mg-0.9Si-0.8Mn alloy (AA2014 grade). *J. Therm. Anal. Calorim.* **2007**, *87*, 247–253. [CrossRef]
25. Jiang, H.; Faulkner, R.G. Modelling of grain boundary segregation, precipitation and precipitate-free zones of high strength aluminium alloys-I. The model. *Acta Mater.* **1996**, *44*, 1857–1864. [CrossRef]
26. Li, H.; Chen, P.; Wang, Z.; Zhu, F.; Song, R.; Zheng, Z. Tensile properties, microstructures and fracture behaviors of an Al-Zn-Mg-Cu alloy during ageing after solution treating and cold-rolling. *Mater. Sci. Eng. A* **2019**, *742*, 798–812. [CrossRef]